Wang *et al. Int J Concr Struct Mater* (2025) 19:72
https://doi.org/10.1186/s40069-025-00809-w

International Journal of Concrete
Structures and Materials

RESEARCH

Open Access

A Refined Model of Viscous Stress for Free Water in Concrete Considering the Characteristics of Pore Structure

Qianfeng Wang[1,2], Xiaofen Wang[2], Xinghua Chen[1,2*], Jie Li[2] and Jinsheng Lei[1,2]

Abstract

This study evaluates the mechanical effects of free water in wet-state concrete under dynamic loading, applying principles from the Stefan effect. A novel model of viscous stress is introduced, incorporating pore structure characteristics for the first time. Pore structure features of both mortar and aggregate are analyzed using mercury intrusion porosimetry. Equations are developed to integrate the differential pore volume and pore diameter of mortar and aggregate, facilitating the calculation of viscosity stress coefficients. A water content model, based on pore structure and water content assessments, is proposed to determine the distribution of unbound water. The results reveal that free water, within the lognormal distribution of pore sizes, fills nearly all available pore volume. However, when pore diameters follow a power law distribution, complete filling is not achievable. The viscous stress induced by pore water is primarily influenced by freely moving water in smaller pores. When free water adheres to apertures within a specific diameter range governed by the power law, substantial viscous stress occurs. The effect of viscous stress on larger pore diameters is negligible compared to the strength of the concrete matrix. The methodology for calculating pore water viscous stress in concrete, a composite material consisting of mortar and aggregate, is clearly outlined, and the improved model aligns well with experimental data.

Keywords Concrete, Pore water, Pore structure characteristics, Stefan effect, Viscous stress

1 Introduction

Concrete is a porous material with many pores, holes, and micro-cracks in its structure. In submerged concrete structures, such as dams and bridge piers, free water infiltrates from the surface to the interior. These moist structures face various loading conditions, including static and impact loads, throughout their operational lifespan. The mechanical properties of concrete can vary under external loads because of unbound water molecules (Kaplan, 1980; Rossi, 1991a, 1991b; Wang et al., 2016a, 2016b; Yan & Lin, 2008). While studies have examined the mechanical properties of wet concrete under various loads, a significant gap remains in quantitative research on free water effects in concrete.

Concrete materials respond sensitively to loading rates, with this behavior influenced by free water in the pores. Free water under quasi-static test conditions can weaken concrete strength. Studies show that higher water content reduces the static compressive strength of concrete (Wang et al. 2007; Wittmann et al., 1987). Conversely, some studies show that saturated concrete has lower tensile strength than dry concrete (Ross et al., 1996; Wang & Li, 2007a, 2007b). Cadoni et al. (2005) found that the dynamic tensile strength of wet and dry concrete specimens exceeded their static tensile strength. At medium

Journal information: ISSN 1976-0485 / eISSN 2234-1315.

*Correspondence:
Xinghua Chen
chenxinghua@ctgu.edu.cn
[1] Hubei Key Laboratory of Disaster Prevention and Mitigation, China Three Gorges University, Yichang 443002, Hubei, China
[2] College of Civil Engineering & Architecture, China Three Gorges University, Yichang 443002, Hubei, China

strain rates (i.e., 10^{-4}/s ~ 10^{-1}/s), Reinhardt et al. (1990) observed that saturated concrete had a higher splitting strength than dry concrete. Zhang et al. (2015) found that loading rate affects dry and saturated concrete, with saturated concrete being more sensitive to strain rate. Rossi (1991a, 1991b) suggested that the increase in dynamic strength of wet concrete is mainly due to free water in the pores. He first introduced the Stefan effect to explain this phenomenon. Subsequently, researchers have used the Stefan effect to explain how the strength of saturated concrete (Rossi & Toutlemonde, 1996; Wang et al., 2009; Zheng, 2004) and rock (Zhou et al., 2016) increases with strain rate. Pedersen et al., (2008, 2013) created a dynamic model based on the Stefan effect to simulate how loading rate and moisture content affect concrete's mechanical properties. Sun et al. (2020) found that the dynamic enhancement factor of concrete correlates with its degree of saturation. The dynamic compressive strength of concrete linearly increases with the fluid's viscosity in its pores. This observation validates the Stefan effect. The study used a viscous liquid and concrete skeleton to examine the Stefan effect, but did not analyze the mechanical effects of the liquid under dynamic loading.

Wet concrete is more sensitive than dry concrete. The accepted explanation for the mechanical mechanism is that the viscous fluid in the pores creates viscous stress under dynamic loads. This stress hinders concrete deformation, increasing its strength. Wu et al. (2012) conducted a dynamic test on moist concrete. The findings showed that higher water content increases the dynamic tensile strength of wet concrete, supporting the mechanical mechanism explanation of the wet concrete rate effect. Some experimental studies struggle to apply the Stefan effect to explain observed data patterns. Wang et al., (2016b) noted that concrete's strain rate sensitivity surpasses that of dry concrete at water pressures of 2 MPa and 5 MPa. Zheng et al. (2021) used liquids of varying viscosity to saturate concrete. The strength increase from a viscous liquid is lower for glycol-saturated concrete than for water-saturated concrete. The increase in concrete strength from a viscous liquid is not directly proportional to its viscosity coefficient. The differing permeability of liquids with various viscosities in concrete pores under natural conditions may explain this phenomenon.

The pore structure of concrete is complex, with diameters ranging from less than 0.01 μm to over 100 μm (Mehta & Monteriro, 2006). Varying fly ash content (Zeng et al., 2012) or water–cement ratios (Li et al., 2019) in concrete leads to greater variability in pore size distribution. Some researches show that different types and quantity of nanofillers (Wang et al., 2021) or surface-modified carbon nanotubes (CNTs) (Wang et al., 2023) are closely related to the pore structure characteristics or fractal dimension. Liang et al. (2020) tested concrete with different fly ash contents under water pressure. Their findings showed that concrete strength enhancement from the same volume of pore water varies with fly ash content. Kaji and Fujiyama (2014) discovered that the rate sensitivity of low water–cement ratio concrete was more pronounced. This phenomenon is due to the viscous stress from unbound water in the pores, closely linked to the structural characteristics of those pores. The Stefan effect states that for a constant volume of pore water, viscous stress increases as pore diameter decreases (Sun et al., 2020; Zheng et al., 2021). Free water adhering to pores of different diameters alters viscous stress. The specific pore size ranges saturated with free water and their water content levels remain uncertain. Examining the concrete pore structure and pore water distribution is essential to understand the dynamic mechanical effects of free water within the pores.

Based on this, a refined model of viscous stress, considering pore structure characteristics, is proposed for the first time in the present study to address total viscous stress in composite porous media under dynamic loading. First, the study presents the viscous stress coefficient of mortar and aggregate based on the pore structure detection results. It explores the pore diameter range, where the free water volume content in the pores of mortar and aggregate is equivalent, and where free water is attached. The study also examined the impact on the viscous stress coefficient and analyzed how the viscous stress changed due to the presence of free water in wet mortar as the pore diameter decreased. The cumulative pore distribution curve of mortar and aggregate is analyzed in a logarithmic coordinate system, segmenting the pore diameter into power law and lognormal distribution ranges. These segments indicate pore size intervals that facilitate or hinder free water infiltration, establishing a model for concrete moisture content. Finally, the method for calculating the pore water viscosity stress of concrete from mortar and aggregate materials, correcting for the effects of different effective fill rates, is presented. The findings of this study provide a basis for the design and safety assessment of concrete structures used in aquatic settings.

2 Refined Model of Viscous Stress Based on Pore Structure Characteristics

2.1 Stefan Effect and its Generalization

The Stefan effect describes the generation of a resistance force F_v that opposes the motion when two parallel plates, separated by a distance h and containing a thin viscous film (e.g., water or oil), are moved apart at speed $\frac{dh}{dt}$ (Rossi, 1991a, 1991b; Sun et al., 2020):

$$F_v = \frac{3\eta V^2}{2\pi h^5}\left(\frac{dh}{dt}\right) \tag{1}$$

where η is the viscosity coefficient of the fluid, V is the volume of the fluid.

Let R be the radius of the fluid between the discs, $V = \pi R^2 h$ the fluid volume, and $A = \pi R^2$ the discs' area. Average viscous stress occurs when the disk is approached and separated at a specific velocity:

$$\sigma_v = \frac{F_v}{A} = \frac{3\eta V^2}{2h^5\pi R^2}\left(\frac{dh}{dt}\right) = \frac{3\eta V}{2\pi h^4}\dot{h} \tag{2}$$

In porous materials, such as concrete and rocks, exposure to water allows free water to infiltrate the pores. Different scholars employ various criteria for classifying voids (Frías & de Rojas, 1997; Kumar & Bhattacharjee, 2003). Aggregates used in concrete show complex and variable pore diameters, as noted in a prior study (Kayyali, 1985). Free water infiltration into complex pore structures, including gel, capillary, and macropores, can cause the formation of pores and micro-cracks in materials, such as mortar and aggregate. This phenomenon arises from the liquid surface tension in the system. The fluid is expected to form a mesoscopic liquid bridge. Dynamic loads on porous media materials with free water in the pores generate viscous stress. The Stefan effect stress hinders the material's skeleton movement, increasing its macroscopic strength. The obstructive force rises with the loading rate.

Equation (2) indicates that the average viscous stress of the fluid under load depends on the distance between the flat plates, not on the disk's radius. The fluid in concrete pores can be modeled as a viscous fluid between discs, with the pore diameter equated to the separation distance, as shown in Fig. 1. The viscous stress from the fluid in the pores under dynamic loading can be expressed as

$$\sigma_v = \frac{3\eta V}{2\pi \phi^4}\dot{\phi} \tag{3}$$

When radial pore deformation occurs alongside the deformation of the concrete skeleton, the strain can be mathematically expressed as

$$\dot{\varepsilon} = \dot{\phi}/\phi \tag{4}$$

Consequently, the average viscous stress of the fluid in the pore under dynamic loading can be expressed as

$$\sigma_v = \frac{3\eta V}{2\pi \phi^3}\dot{\varepsilon} \tag{5}$$

Pores in the concrete skeleton are randomly distributed, causing the viscous stress from adhering fluid to vary in multiple directions. In three-dimensional space, the viscous stress from the fluid in each direction is assumed to be one-third of the total pore volume. Thus, the viscous stress from the fluid in each direction can be expressed as

$$\tilde{\sigma}_v = \frac{3\eta}{2\pi}\frac{V/3}{\phi^3}\dot{\varepsilon} = \frac{\eta}{2\pi}\frac{V}{\phi^3}\dot{\varepsilon} \tag{6}$$

Analysis of Eq. (6) shows that increased fluid volume raises viscous stress due to fluid adherence to pore spaces. This phenomenon can enhance concrete strength.

Viscous stress is linearly related to fluid volume and inversely proportional to the cube of the pore diameter. Pore diameter is expected to have a greater impact on viscous stress than fluid volume. It is crucial to aggregate the viscous stress from a viscous fluid across various pore diameters to evaluate its cumulative mechanical impact.

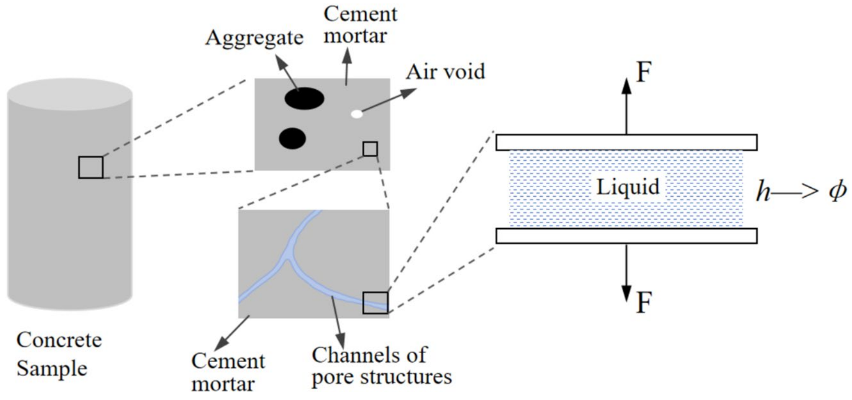

Fig. 1 Evolution of concrete porosity with a diagram of idealized pores (from macro to micro scale)

2.2 Establishment of a Refined Model for Viscous Stress

Fig. 2 illustrates the cumulative pore volume as a function of pore diameter for mortar. Assuming a pore diameter range of $[a, b]$, divided into n equal parts, the viscous stress induced by the viscous fluid adhered to each pore diameter interval $[\phi_i, \phi_{i+1}]$ is calculated. The total viscous stress from fluid on different pore diameters is the sum of the viscous stress in each micro-element.

If the differential of pore volumes and pore diameters (DPVPD) is denoted as $V'(\phi)$, then the corresponding pore volume for micro-elements within the pore diameter interval $[\phi_i, \phi_{i+1}]$ is represented as $\Delta V = (\phi_i - \phi_{i+1}) \cdot V'(\phi)$.

Based on Eq. (6), as the distributed interval of the viscous fluid decreases from ϕ_{i+1} to ϕ_i, the viscous stress increment is

$$\Delta\tilde{\sigma}_v = \frac{\eta}{2\pi}\frac{V'(\overline{\phi})(\phi_i - \phi_{i+1})}{\overline{\phi}^3}\dot{\varepsilon} = \frac{\eta}{2\pi}\frac{V'(\overline{\phi})\frac{b-a}{n}}{\overline{\phi}^3}\dot{\varepsilon} \quad (7)$$

in which $\overline{\phi}$ is the average pore diameter for the interval $[\phi_i, \phi_{i+1}]$.

When the viscous stress resulting from the viscous fluid in each pore diameter interval accumulates, the total viscous stress caused by all viscous fluids can be determined:

$$\tilde{\sigma}_v = \frac{\eta}{2\pi}\dot{\varepsilon}\sum\left(\frac{V_1'(\phi)\frac{b-a}{n}}{\phi_1^3} + \cdots + \frac{V_i'(\phi)\frac{b-a}{n}}{\phi_i^3} + \cdots + \frac{V_n'(\phi)\frac{b-a}{n}}{\phi_n^3}\right) \quad (8)$$

when n is large enough, the range of the pore diameter interval approaches zero, then there is

$$\tilde{\sigma}_v = \frac{\eta}{2\pi}\dot{\varepsilon}\lim_{n\to\infty}\sum_{i=1}^{n}\left(\frac{V_i'(\phi)}{\phi_i^3}\frac{b-a}{n}\right) \quad (9)$$

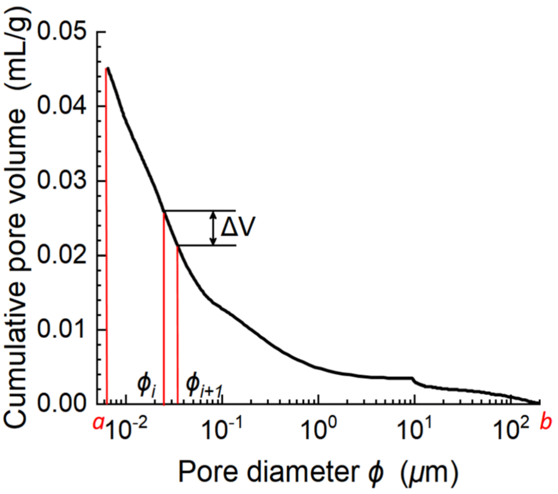

Fig. 2 Schematic diagram of cumulative pore volume and micro-elements

Expressed by integral form

$$\tilde{\sigma}_v = \frac{\eta}{2\pi}\dot{\varepsilon}\int_a^b \frac{V'(\phi)}{\phi^3}d\phi \quad (10)$$

where ϕ is the pore diameter; $V'(\phi)$ is the DPVPD, which is directly provided by the testing data of the mercury porosimetry. $V'(\phi)$ is denoted by Dv_ϕ hereinafter. Thus, Eq. (10) also can be expressed by

$$\tilde{\sigma}_v = \frac{\eta}{2\pi}\dot{\varepsilon}\int_a^b \frac{Dv\_\phi}{\phi^3}d\phi \quad (11)$$

In Eq. (11), the unit of Dv_ϕ is cc/(μm·g), and the mass is measured in grams. Equation (11) enables the determination of the viscous stress induced by the viscous fluid within each gram of porous media material subjected to dynamic loading.

2.3 Viscous Stress Coefficient

Equation (11) indicates that viscous stress in a fluid is mainly linked to its viscosity coefficient (η), strain rate, and pore structure characteristics. The integral expression of pore structure characteristics denotes the viscous stress coefficient (*VSC*) for porous media:

$$VSC = \frac{1}{2\pi}\int_a^b \frac{Dv\_\phi}{\phi^3}d\phi \quad (12)$$

The study pertains to the DPVPD and the range of pore diameters within which fluid is contained. Consequently, the viscous stress generated by the fluid within the pore spaces can be formulated as

$$\tilde{\sigma}_v = \eta\dot{\varepsilon} \cdot VSC \quad (13)$$

From Eq. (12), the key step in the calculation is obtaining the DPVPD (Dv_ϕ), determined through mercury porosimetry testing of porous materials. Viscous stress at different strain rates is calculated based on the liquid type in the porous medium by determining the viscosity coefficient (η) and applying Eq. (13). Viscous stress is the stress generated by a viscous fluid due to dynamic loading per gram of porous media. Determining the viscosity coefficient (η) of a fluid is essential for the type of liquid in the porous medium. Viscous stress at different strain rates can be calculated using Eq. (13). This equation describes the dynamic load from the viscous fluid in the porous medium per gram of viscous stress.

As Dv_ϕ is directly derived from the supporting software of the mercury porosimetry test, its unit is cc/(μm·g), where 1 cc is equivalent to 1 cm^3 or 1 mL. In Eq. (12), the integral involves pore diameter in micrometers (μm) and Dv_ϕ in cc/(μm·g), leading to non-uniform units of length. After conducting dimensional analysis, to make the units consistent and obtain accurate results in SI units, the precise VSC is obtained by multiplying the result of Eq. (12) by 10^{12} when the unit of ϕ is expressed by micrometers (μm) and the Dv_ϕ is expressed by cc/(μm·g). This adjustment serves to mitigate the impact of varying units during the calculated process.

2.4 Viscous Stress for Composite Material of Porous Media

In composite materials with diverse porous media, the viscous stress from the fluid in the pores under dynamic loading can be calculated using the weighted volume fraction of each material:

$$\overline{\sigma}_v = \sum_{i=1}^{n} p_i \cdot \sigma_{v\_i} \tag{14}$$

in which p_i indicates the volume proportion of the ith component in the composite; σ_{v_i} represents the pore water viscous stress $\sigma_{v\_i} = \rho_i \tilde{\sigma}_{v\_i}$ induced by the ith component material per unit volume; and ρ_i stands for the density of the ith component material in the composite material.

3 Case Study for Concrete

3.1 Test Sample

Raw materials for concrete production include P·O 42.5 Ordinary Portland cement, coarse aggregate, and tap water. This aggregate includes small stones (5 ~ 20 mm) and medium stones (20 ~ 40 mm). The coarse aggregate consists of graded granite crushed stone with a particle size of 5 ~ 40 mm and an apparent density of 2,690 kg/m^3. The fine aggregate is natural river sand, with an apparent density of 2,580 kg/m^3 and a fineness modulus of 2.3, classified as medium sand. Tap water is recommended for mixing with FDN high-efficiency water reducer. The concrete has a water–cement ratio of 0.45, with quantities of cement, water, sand, and water reducer listed in Table 1.

Table 1 Concrete mix ratio (kg/m^3)

Cement	Water	Sand	Small stone	Medium stone	Water reducer
342.85	154.20	639.79	519.58	743.58	2.72

On the same day, three cylindrical mortar specimens measuring 150 × 300 mm were prepared. The concrete is blended using a standard forced mixer, then poured into a cylindrical steel mold. Subsequently, it is vibrated and compacted on a vibrating table.

Molds were removed and labeled after 24 h at room temperature. The specimens were transferred to a standard curing room at 20 ± 2 ℃ and at least 95% relative humidity for 28 days before being placed in a natural environment. After removal from the curing room, concrete specimens will be placed in a natural atmosphere to develop and stabilize porosity, typically taking over 90 days (Zeng et al., 2012).

After 90 days of curing, the compressive strength of dry concrete under static load is 48.3 MPa. The average mass of six concrete specimens is 12.848 kg, and three mortar specimens average 11.879 kg, both in a dry environment. Concrete has an average density of 2,425 kg/m^3, and mortar has an average density of 2,242 kg/m^3. Once the mass of the concrete specimen and the densities of the aggregate and mortar are known, their volumes can be calculated. The concrete specimen consists of 40.79% aggregate and 59.21% mortar.

3.2 Pore Structure Testing

This investigation employed a fully automated mercury porosimeter (Pore Master 33GT) to analyze the pore structure of mortar and aggregate, measuring pore diameters from 6.5 nm to 226 μm. Solid particle diameter in the mercury porosimeter sample tube must not exceed 1.5 cm. The first step is to cut a semicircular sample about 1.5 cm thick from a height between 2/5 and 3/5 of the concrete specimen, as shown in Fig. 3a. Gently tap the mortar and aggregate particles with a small hammer, keeping the diameter under 1.5 cm. Finally, choose particles for the sample tube, prioritizing larger diameters. Before testing, the sample is frozen with liquid nitrogen and sealed for storage, as shown in Fig. 3b.

The cumulative pore volume (CPV) curves of mortar and aggregate are depicted in Fig. 4. The total CPV of mortar and aggregate per gram particle is 0.0451 mL/g and 0.0040 mL/g, respectively. In a unit volume of mortar and aggregate, the total pore volumes V_m^{pore} and V_g^{pore} should be multiplied by the density of the mortar ρ_m and the density of the aggregate ρ_g, respectively, based on the cumulative pore volume. This method facilitates the determination of the porosity of both the mortar and aggregate. The porosity of the mortar P_{m} is 10.111%, while the porosity of the aggregate P_g is 1.076%. The total pore volume and porosity of the mortar component in concrete significantly exceed those of the aggregate component.

3.3 Water Content Test

In low humidity, the six concrete specimens show an average water absorption mass of 54.67 g, resulting

(a) A sample with a thickness of 1.5 cm.

(b) Particle sample with a particle size of 1 ~ 1.5 centimeters

Fig. 3 Particle sample preparation for the detection of pore structure

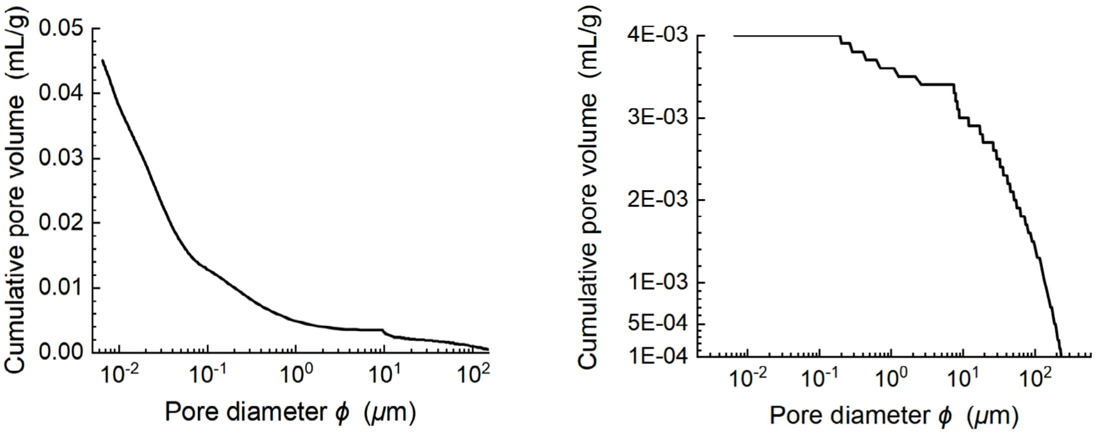

(a) mortar

(b) aggregate

Fig. 4 Cumulative pore volume curves

in an average volumetric moisture content (VWC) of 1.032% and a mass moisture content (MWC) of 0.425%. Concrete saturates with water when exposed to the atmosphere under constant pressure. The process and methodology align with those in the research by Wang et al., (2016b). At water pressures of 3 MPa and 5 MPa, the concrete samples absorbed an average of 12.25 g and 14.71 g of water, leading to VWC increases of 0.231% and 0.278%, respectively.

The water absorption masses of three mortar specimens are 74 g, 72 g, and 76 g, respectively, in atmospheric water environment, so the MWC of the mortar is 0.623%. For the aggregate, first dry it at a temperature of 105 °C, and then soak it in water until the mass remains unchanged. The MWC of the aggregate is 0.10%, and the VWC is 0.269%.

Water content testing has shown that free water cannot fill all pore spaces under atmospheric ambient conditions, comparing to the CPV of and aggregate according to the pore structure testing in Sect. 3.2.

3.4 VSC of Mortar and Aggregate

3.4.1 Differential of Pore Volumes and Pore Diameters (DPVPD)

The essential step in determining the pore water VSC involves acquiring the differentials of pore volumes and pore diameters, denoted as Dv_ϕ. According to the results of mercury porosimetry testing on the pore structure of mortar and aggregate, the pore structure Dv_ϕ of mortar and aggregate is illustrated in Figs. 5 and 6.

3.4.2 VSC of Mortar

The minimum pore diameter of mortar through which pore water can penetrate under water pressure is approximately 0.03 μm (Zhao et al., 2023). In conjunction with the analysis presented in Fig. 5, it has been observed that mutation points and significant inflection points exist within the range of free water penetration associated with the pore diameter range. For this reason, the relationship between Dv_ϕ and ϕ is established in three parts for the pore diameters greater than

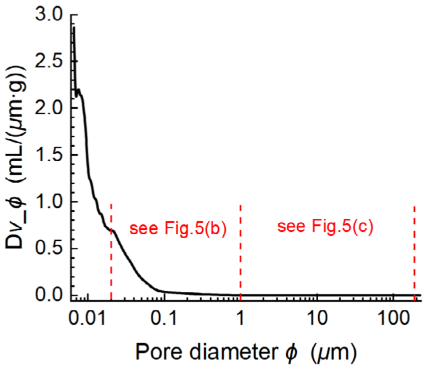

(a) 6.5 nm≤ϕ ≤226 μm

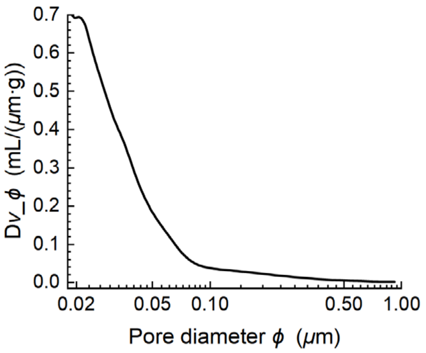

(b) 0.02 μm≤ϕ ≤1.0 μm

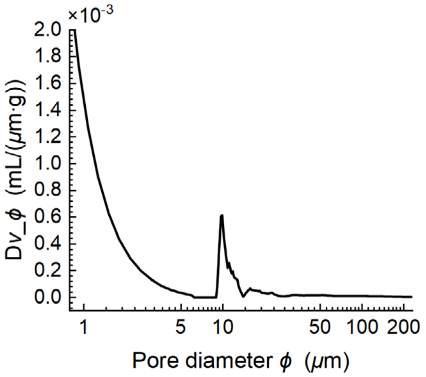

(c) 1.0 μm≤ϕ ≤226 μm

Fig. 5 Differential of pore volumes and pore diameters for mortar

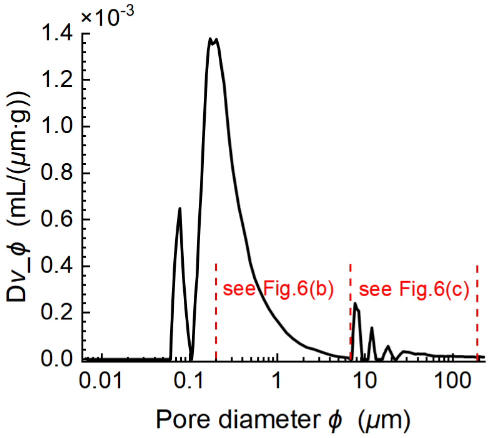

(a) 6.5 nm≤ϕ ≤226 μm

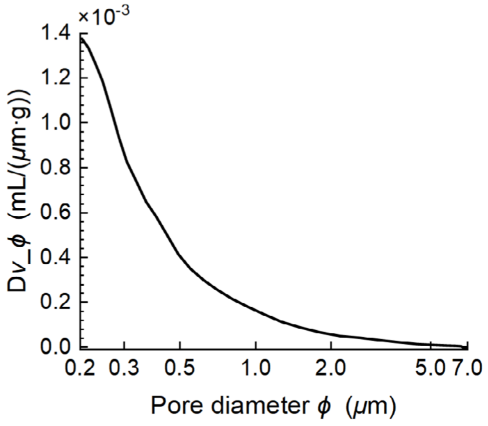

(b) 0.2 μm≤ϕ ≤7 μm

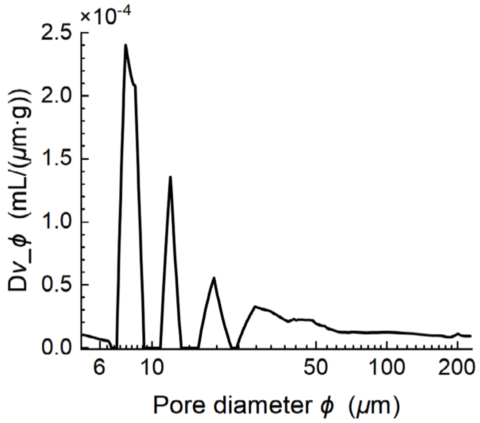

(c) 5 μm≤ϕ ≤226 μm

Fig. 6 Differential of pore volumes and pore diameters for aggregate

0.02 μm, and the expression used for fitting is shown in Eq. (15). The fitting relationship is shown in Fig. 7. The pore diameter range of 0.02 ~ 0.1 μm, 0.1 ~ 6.0 μm, and 9.7 ~ 226 μm of Dv_ϕ can be fitted by Eqs. (15a), (15b), and (15c), respectively, and the relationship curves shown in Fig. 7a, b, and c with the corresponding correlation coefficients were 0.9997, 0.9999, and 0.9807, respectively. It should be noted that for the pore diameter range of 6.0 μm ~ 9.7 μm, Dv_ϕ of the mortar decreased from the maximum value to 0, so this range was not considered:

$$Dv\_\phi = 0.270 - \frac{6.298\times10^{-2}}{\phi} + \frac{5.419\times10^{-3}}{\phi^2} - \frac{1.686\times10^{-4}}{\phi^3} + \frac{2.538\times10^{-6}}{\phi^4} - \frac{1.509\times10^{-8}}{\phi^5} \tag{15a}$$

$(0.02\mu m \le \phi \le 0.1\mu m)$

$$Dv\_\phi = -1.999\times10^{-5} - \frac{1.625\times10^{-4}}{\phi} + \frac{1.937\times10^{-3}}{\phi^2} - \frac{2.679\times10^{-4}}{\phi^3} + \frac{1.132\times10^{-5}}{\phi^4} \tag{15b}$$

$(0.1\mu m \le \phi \le 6.0\mu m)$

$$Dv\_\phi = -8.538\times10^{-6} + \frac{3.965\times10^{-3}}{\phi} - \frac{0.273}{\phi^2} + \frac{8.649}{\phi^3} - \frac{120.267}{\phi^4} + \frac{622.603}{\phi^5} \tag{15c}$$

$(9.7\mu m \le \phi \le 226\mu m)$

By substituting the three appropriate equations of Eq. (15) into Eq. (12) individually, the VSC in three distinct pore diameter ranges for the mortar is determined:

$$VSC_m = \frac{1}{2\pi}\left[-\frac{0.270}{2\phi^2} + \frac{6.298\times10^{-2}}{3\phi^3} - \frac{5.419\times10^{-3}}{4\phi^4} + \frac{1.686\times10^{-4}}{5\phi^5} - \frac{2.538\times10^{-6}}{6\phi^6} + \frac{1.509\times10^{-8}}{7\phi^7}\right]\Bigg|_{a=\phi_{\min}}^{b=\phi_{\max}} \tag{16a}$$

$(0.02\mu m \le \phi \le 0.1\mu m)$

$$VSC_m = \frac{1}{2\pi}\left[\frac{1.999\times10^{-5}}{2\phi^2} + \frac{1.625\times10^{-4}}{3\phi^3} - \frac{1.937\times10^{-3}}{4\phi^4} + \frac{2.679\times10^{-4}}{5\phi^5} - \frac{1.132\times10^{-5}}{6\phi^6}\right]\Bigg|_{a=\phi_{\min}}^{b=\phi_{\max}} \tag{16b}$$

$(0.02\mu m \le \phi \le 0.1\mu m)$

$$VSC_m = \frac{1}{2\pi}\left[\frac{8.538\times10^{-6}}{2\phi^2} - \frac{3.965\times10^{-3}}{3\phi^3} + \frac{0.273}{4\phi^4} - \frac{8.649}{5\phi^5} + \frac{120.267}{6\phi^6} - \frac{622.603}{7\phi^7}\right]\Bigg|_{a=\phi_{\min}}^{b=\phi_{\max}} \tag{16c}$$

$(9.7\mu m \le \phi \le 226\mu m)$

where $a = \phi_{\min}$ and $b = \phi_{\max}$ are the maximum and minimum values of the pore diameter attached by the viscous liquid (such as free water), respectively.

3.4.3 VSC of Aggregate

Combined with the analysis of Figs. 6a and 4b, it is found that there is an obvious and especial turning point at pore diameter of 0.2 μm for the aggregate. The relationship between Dv_ϕ and ϕ of the aggregate is calculated in two parts. Like mortar, in the pore diameter range of 7.0 μm ~ 7.2 μm, the Dv_ϕ value of aggregate decreases from the maximum value to 0, which is not considered. The expression used for fitting is shown in Eq. (17) and the fitting curve is shown in Fig. 8. The pore diameter range of 0.2 ~ 7.0 μm and 7.2 ~ 226 μm of Dv_ϕ can be fitted by Eqs. (17a) and (17b), respectively, and the relationship curves shown in Fig. 8a, b with the corresponding correlation coefficients were 0.9996 and 0.9992, respectively:

$$Dv\_\phi = -3.093\times10^{-5} + \frac{2.082\times10^{-4}}{\phi} - \frac{4.738\times10^{-5}}{\phi^2} + \frac{3.554\times10^{-5}}{\phi^3} - \frac{4.597\times10^{-6}}{\phi^4} \tag{17a}$$

$(0.2\mu m \le \phi \le 7.0\mu m)$

$$Dv\_\phi = 4.388\times10^{-6} + \frac{1.099\times10^{-3}}{\phi} - \frac{4.415\times10^{-2}}{\phi^2} + \frac{1.420}{\phi^3} - \frac{13.480}{\phi^4} + \frac{42.284}{\phi^5} \tag{17b}$$

$(7.2\mu m \le \phi \le 226\mu m)$

Substituting the two fitting equations of Eq. (17) into Eq. (12), respectively, the VSCs in two different pore diameter ranges for the aggregate are obtained:

$$VSC_g = \frac{1}{2\pi}\left[\frac{3.093\times10^{-5}}{2\phi^2} - \frac{2.082\times10^{-4}}{3\phi^3} + \frac{4.738\times10^{-5}}{4\phi^4} - \frac{3.554\times10^{-5}}{5\phi^5} + \frac{4.597\times10^{-6}}{6\phi^6}\right]\Bigg|_{a=\phi_{\min}}^{b=\phi_{\max}} \tag{18a}$$

$$(0.2\mu m \le \phi \le 7.0\mu m)$$

$$(7.2\mu m \le \phi \le 226\mu m)$$

$$VSC_g = \frac{1}{2\pi}\left[-\frac{4.388\times10^{-6}}{2\phi^2} - \frac{1.099\times10^{-3}}{3\phi^3} + \frac{4.415\times10^{-2}}{4\phi^4} - \frac{1.420}{5\phi^5} + \frac{13.480}{6\phi^6} - \frac{42.284}{7\phi^7}\right]\Bigg|_{a=\phi_{\min}}^{b=\phi_{\max}} \tag{18b}$$

where $a = \phi_{\min}$ and $b = \phi_{\max}$ are the maximum and minimum values of the pore diameter attached by the viscous liquid (such as free water), respectively.

3.5 Viscous Stress of Wet Concrete

Concrete consists of mortar and aggregate, exhibiting variations in the pore water viscous stress between these two constituents. The total viscous stress, denoted as $\overline{\sigma}_{v\_con}$, induced by pore water in wet concrete is determined by considering the volume ratio of mortar to aggregate:

$$\overline{\sigma}_{v\_con} = p_m \cdot \rho_m \cdot \tilde{\sigma}_{v\_m} + p_g \cdot \rho_g \cdot \tilde{\sigma}_{v\_g} \tag{19a}$$

$$\overline{\sigma}_{v\_con} = p_m \cdot \sigma_{v\_m} + p_g \cdot \sigma_{v\_g} \tag{19b}$$

$$\overline{\sigma}_{v\_con} = \left(p_m \cdot \rho_m \cdot VSC_m + p_g \cdot \rho_g \cdot VSC_g\right)\eta\dot{\varepsilon} = \overline{VSC} \cdot \eta\dot{\varepsilon} \tag{20}$$

$$\overline{VSC} = p_m \cdot \rho_m \cdot VSC_m + p_g \cdot \rho_g \cdot VSC_g \tag{21}$$

where p_m and p_g represent the volume proportions of mortar and aggregate in concrete, $\tilde{\sigma}_{v\_m}$ and $\tilde{\sigma}_{v\_g}$ denote the viscous stress induced by fluid (free water) in each gram of mortar and aggregate. In addition, σ_{v_m} represents the viscous stress induced by the fluid (free water) in the mortar, while σ_{v_g} denotes the viscous stress caused by the fluid in the aggregate per unit volume. In addition, VSC_m and VSC_g represent the viscous stress coefficients of the mortar and aggregate per unit mass, respectively, while $\overline{VSC}$ denotes the viscous stress coefficient per unit volume of concrete.

4 Results and Discussion

4.1 Factors Influencing the Viscous Stress Coefficient

4.1.1 Effect of the DPVPD

From Eqs. (12) and (13), it can be inferred that the viscous stress induced by pore water is intricately linked to the VSC. The VSC is primarily associated with the pore structural characteristics and the distribution diameter range of free water. Figure 9 illustrates a comparison of the fitting curves for mortar and aggregate when the pore diameter exceeds 0.1 μm. These curves represent the fitting results derived from the test data on pore structure characteristics. The VSC discusses the attachment of

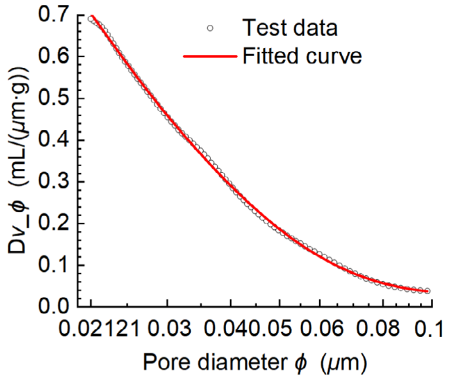

(a) 0.02 μm ~ 0.1 μm

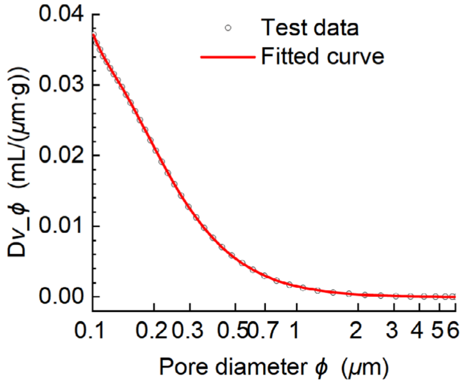

(b) 0.1 μm ~ 6.0 μm

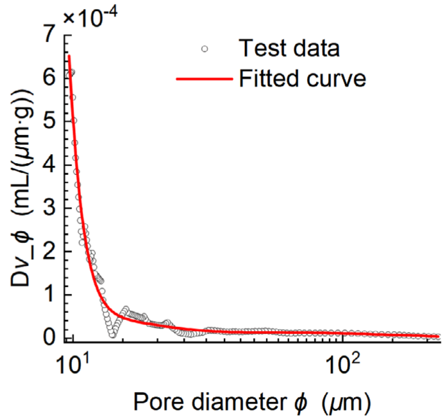

(c) 9.7 μm ~ 226 μm

Fig. 7 Relationship curve between *Dv_ϕ* and *ϕ* with mortar pore diameter greater than 0.02 μm viscous liquid (such as free water) to different pore diameter ranges. When free water adheres to the same pore diameter range, the greater the DPVPD, the larger the corresponding pore volume, resulting in a larger VSC.

In Fig. 9a, the DPVPD of mortar being 2.72 times that of aggregate in the pore diameters between 4.0 μm and 6.0 μm. Similarly, when the pore diameter ranges from 0.2 μm to 1.0 μm, the VSC of mortar is 14.25 times that of aggregate. When the pore diameter range is consistent, a greater difference in pore diameter results in a higher pore water volume. It is evident that the DPVPD of the mortar exceeds that of the aggregate, indicating that the pore volume in the mortar is greater than in the aggregate. The viscous stress coefficient of mortar is higher than that of aggregate.

In Fig. 9b, the intersection point of the pore volume differentials of aggregate and mortar is 12.0 μm. When the pore diameter ranges from 12.0 μm to 226 μm, the VSC in mortar is smaller than that of aggregate. In the pore diameter range of 7.41 μm to 12.0 μm, the VSC of mortar exceeds that of aggregate.

4.1.2 Effect of Pore Diameter

When the viscous fluid sticks to the pore space with a diameter of $\phi^* \sim 0.08$ μm, and the range of ϕ^* changes between 0.02 μm and 0.08 μm. The variation trend of the viscous stress coefficient of the mortar with ϕ^* in different coordinates is shown in Fig. 10.

Figure 10a shows that as the pore diameter decreases, the value continues to rise. When $\phi^* \leq 0.04$ μm, the acceleration of the increase speed is significant. This demonstrates that viscous fluid can generate higher viscous stress in narrower pore diameters. In Fig. 10b, it is evident that in the logarithmic coordinate system, the viscous stress coefficient decreases linearly as the pore diameter increases. The relationship between the two can be expressed by Eq. (22) or Eq. (23). The pore diameter ranges from 0.02 μm to 0.08 μm, and the relationship between the viscous stress coefficient and the pore size follows a power law distribution.

$$\log VSC_m = \log s - t \log \phi \tag{22}$$

$$VSC_m = s \cdot \phi^{-t} \tag{23}$$

where "s" and "t" represent fitting parameters, $s = 6.215 \times 10^7$, $t = 3.63184$. The results under bilinear and double logarithmic coordinates are displayed in Fig. 11.

Power-law distribution is a commonly used probability distribution in social and natural sciences. Social networks (Stephen & Toubia, 2009) and city sizes (Gangopadhyay & Basu, 2009) display a networked connection pattern with an uneven distribution of node sizes, following a power-law distribution. In natural science, earthquakes of various magnitudes follow a power-law distribution (Kagan, 2010), while events such as floods and heavy rains are also often characterized by power-law distributions (Malamud & Turcotte, 2006). A popular saying is the 80/20 rule, also known as the Pareto rule (Newman, 2005).

This law shows that about 20% of factors drive 80% of outcomes, indicating that the "critical few" significantly influence results more than the "majority." The study created a refined model of viscous stress and examined pore structure characteristics. Viscous fluids, like water in mortar pores, create significant stress mainly in smaller pores.

4.2 Mechanical Effects of Free Water in Mortar and Aggregate Pore Diameters

In discussing the impact of pore diameter range on viscous stress, we assume that mortar and aggregate have 10% of pore space filled with free water, equating to 0.0045 mL of free water per gram of mortar, and 0.0004 mL of free water in the pores of a gram of aggregate, but the attached pore diameter range varies.

To analyze the viscous stress caused by the same volume of pore water in mortar and aggregate, the viscous stress $\tilde{\sigma}_v$ is divided by the volume of pore water V_w^{pore} to obtain the dynamic coefficient of pore water D_w^{pore}, that is expressed by

$$D_w^{pore} = \frac{\tilde{\sigma}_v}{V_w^{pore}} \tag{24}$$

The D_w^{pore} comparison of pore water in mortar and aggregate in different pore diameter intervals is shown in Fig. 12. D_w^{pore} of pore water in aggregate is less than that in mortar when pore diameters greater than 8 μm, while D_w^{pore} in aggregate is higher than that in mortar when pore diameter range of approximately 0.2 ~ 8 μm. In general, the smaller the pore diameter, the larger D_w^{pore}, which indicates that when the same volume of pore water is attached to different pore diameter, the viscous stress caused by pore water will be different. Therefore, for porous media materials like concrete, a comprehensive analysis of the effect of total pore water content on their dynamic mechanical properties is essential. The dynamic viscous stress caused by pore water should be closely linked to the material's pore structure characteristics for analysis.

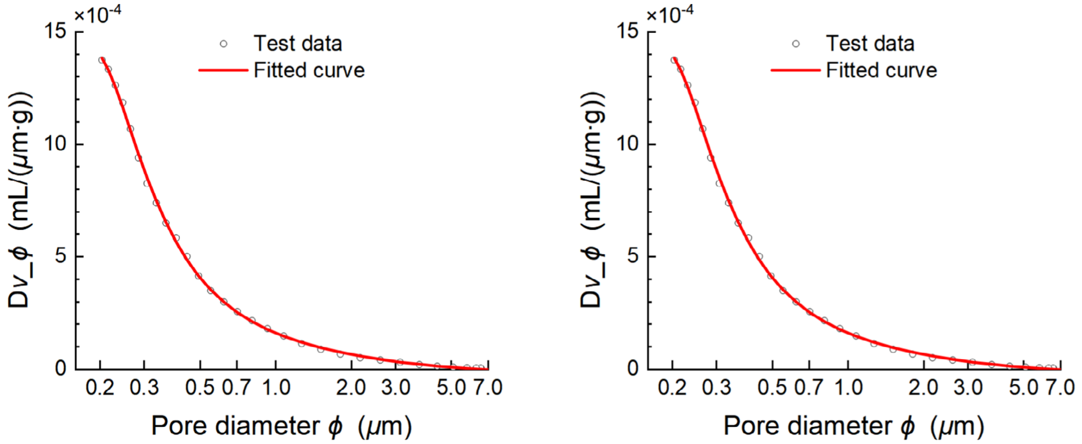

(a) 0.2 μm ~ 7.0 μm (b) 7.2 μm ~ 226 μm

Fig. 8 Relationship curve between *Dv_ϕ* and *ϕ* with the aggregate pore diameter greater than 0.2 μm

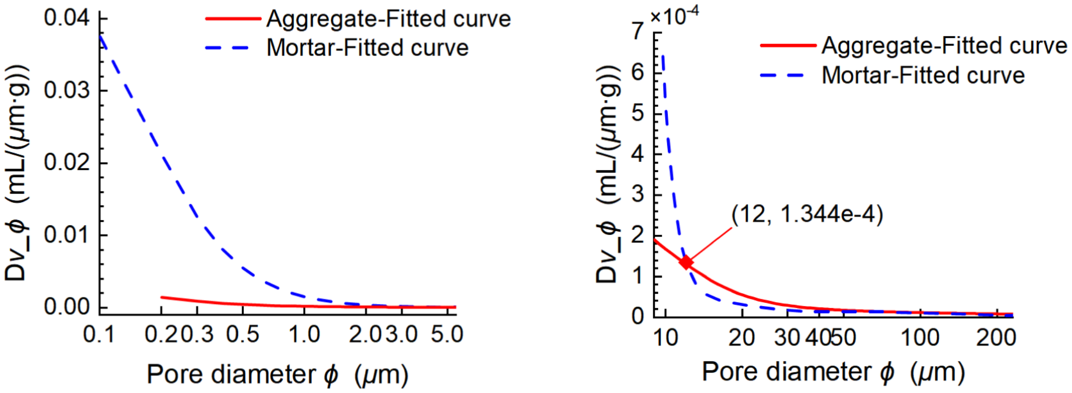

(a) 0.1 μm ~ 8.0 μm (b) 8.0 μm ~ 226 μm

Fig. 9 Comparison of fitted curves between DV _φ and φ of pore diameter greater than 0.1 μm for mortarand aggregate

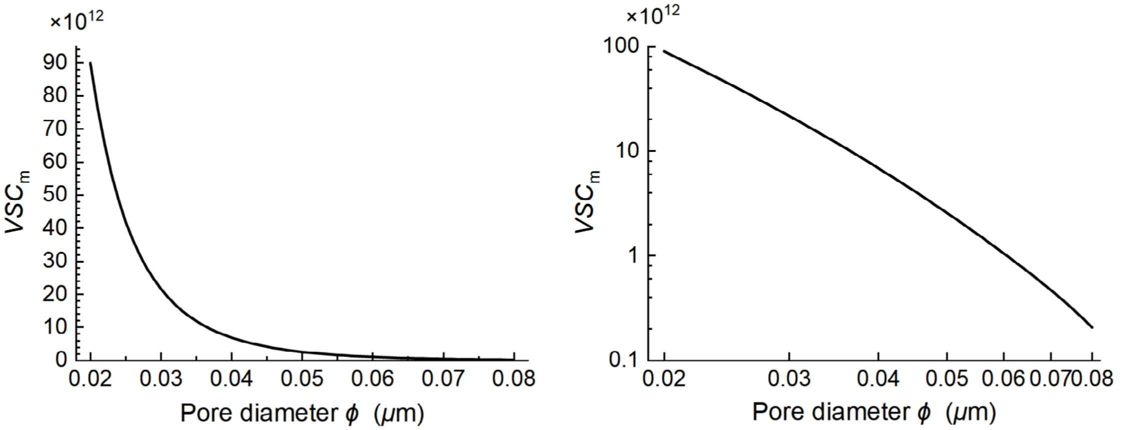

(a) Bilinear coordinates (b) Double logarithmic coordinates (log-log)

Fig. 10 Relationship between pore water viscous stress coefficient and pore diameter

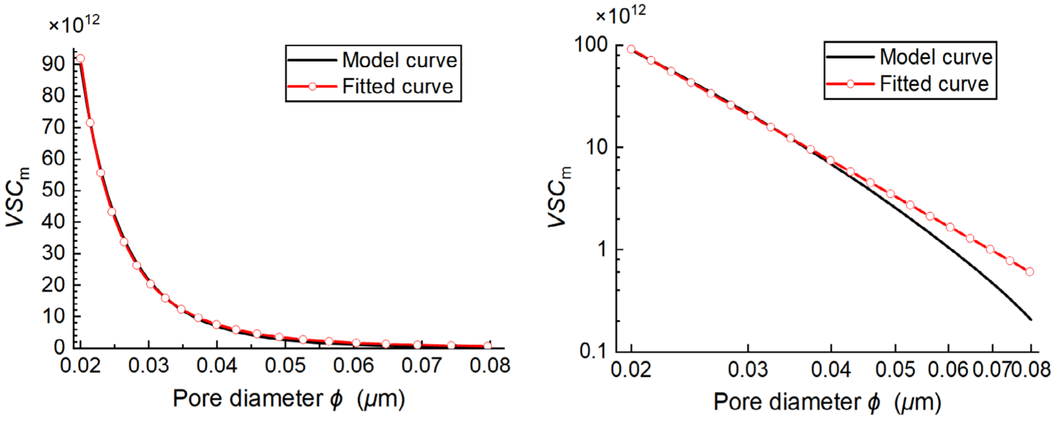

(a) Bilinear coordinate (b) Double logarithmic coordinates (log-log)

Fig. 11 Comparison of fitting curves between the viscous stress coefficient of mortar and pore diameter

4.3 Probabilistic Characteristics of Pore Structure and Free Water Distribution

Concrete absorbs water in natural environments, but it is crucial to assess whether water can completely fill all pore spaces. During concrete mixing, a limited number of pores are incorporated into the mortar, and admixtures are added to introduce tiny air bubbles. Entrapped air voids can reach 3 mm, while entrained air bubbles range from 50 to 300 μm (Mehta & Monteriro, 2006). Air in the interconnected pores hinders free water infiltration. As water content increases, air pressure in the pores rises, creating a barrier to free water entry into narrower spaces. Larger-diameter pores are more likely to contain free water. Capillary pores have irregular shapes. In high water–cement ratio mortars, capillary pore diameters can reach 3–5 μm. Free water can be absorbed and retained via capillary action on pore surfaces. The gel pore diameter of interlayer pores in calcium–silicate–hydrates (C–S–H) ranges from 3 to 4 nm and features rough surfaces (Mehta & Monteriro, 2006). This characteristic prevents free water infiltration, making them "non-wetting" and hard to saturate. Types of pores include through, intersecting, blind, and closed pores (Giesche, 2006). These discontinuous pores often connect larger pores to several smaller ones. Air obstructs water movement in small pores. Wang et al., (2016b, 2017) identified a positive correlation between water pressure and concrete water content. This shows that under certain water pressure conditions, free water cannot fully occupy all pore spaces in concrete.

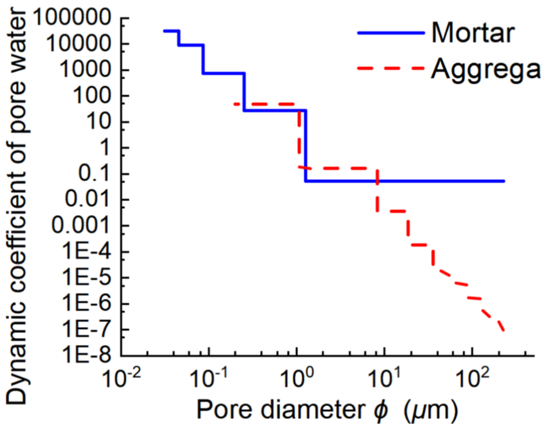

Fig. 12 Comparison chart of dynamic coefficient of pore water in mortar and aggregate

The cumulative porosity curve of mortar and aggregate in logarithmic coordinates is represented as a dashed line in Fig. 13.

Figure 13 indicates that these curves are similar. The curve resembles an arc for larger pore diameters and a straight line for smaller ones. The larger pore diameters follow a lognormal distribution, while the smaller ones follow a power law distribution. Fitting the cumulative pore volume (CPV) establishes equations. Equations (25) and (26) are derived for the mortar and aggregate components in various sections. By integrating Fig. 13 with Eqs. (25) and (26), the mortar's pore characteristics show a logarithmic normal distribution and a power law function. The dividing diameter is roughly 1.25 μm for mortar and 7.0 μm for aggregate.

For mortar, the *CPV* fitting curves were performed over pore diameter ranges of 1.25 ~ 226 μm, 0.15 ~ 1.25 μm, 0.02 ~ 0.15 μm, and 0.0065 ~ 0.02 μm using Eqs. (25a), (25b), (25c), and (25d), respectively, with correlation coefficients of 0.9972, 0.9991, 0.9984 and 0.9995, respectively.

For aggregate, the *CPV* fitting curves were conducted over pore diameter ranges of 7.00 ~ 226 μm and 0.20 ~ 7.0 μm using Eqs. (26a) and (26b), respectively,

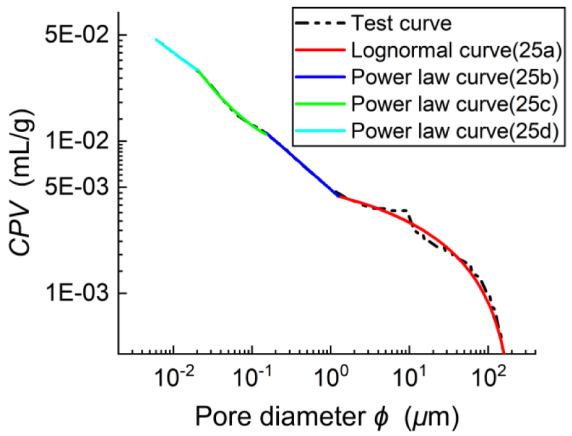

(a) mortar

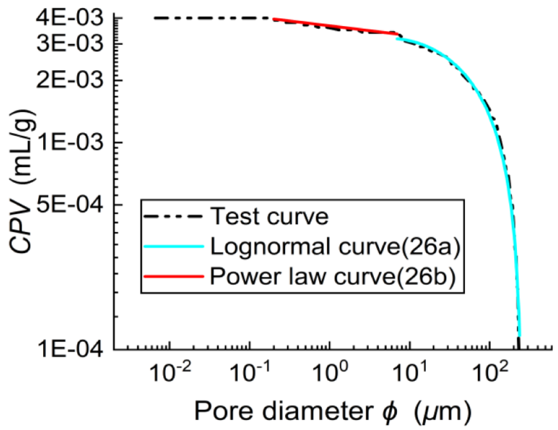

(b) aggregate

Fig. 13 CPV curves of mortar and aggregate and their fitting curves in logarithmic coordinate system

with corresponding correlation coefficients of 0.9951 and 0.9737, respectively:

$$CPV_{m\_lognormal} = -0.055 + 0.061 \cdot \exp\left[-\frac{1}{2}\left(\frac{\ln(\phi/0.006)}{23.401}\right)^2\right] \tag{25a}$$

$$(1.25\mu m \le \phi \le 226\mu m)$$

$$CPV_{m\_powelaw} = -0.116 \times 10^{-3} + 0.494 \times 10^{-2} \cdot \phi^{-0.446} \ (0.15\mu m \le \phi \le 1.25\mu m) \tag{25b}$$

$$CPV_{m\_powelaw} = 0.736 \times 10^{-2} + 0.692 \times 10^{-3} \cdot \phi^{-0.888} \ (0.02\mu m \le \phi \le 0.15\mu m) \tag{25c}$$

$$CPV_{m\_powelaw} = 0.369 \times 10^{-2} + 0.483 \times 10^{-2} \cdot \phi^{-0.427} \ (0.0065\mu m \le \phi \le 0.02\mu m) \tag{25d}$$

$$CPV_{g\_lognormal} = -0.142 + 0.145 \cdot \exp\left[-\frac{1}{2}\left(\frac{\ln(\phi/5.332)}{18.302}\right)^2\right] \tag{26a}$$

$$(7.0\mu m \le \phi \le 226\mu m)$$

$$CPV_{g\_powelaw} = 0.314 \times 10^{-2} + 0.434 \times 10^{-3} \cdot \phi^{-0.385} \ (0.20\mu m \le \phi \le 7.0\mu m) \tag{26b}$$

$$CPV_{g\_powelaw} = 4.0 \times 10^{-3} \ (0.0065\mu m \le \phi \le 0.02\mu m) \tag{26c}$$

Fig. 13 compares the fitting curve to the experimental data for both materials. Both the lognormal distribution and power law functions effectively characterize the cumulative pore volume of mortar and aggregate.

The variable *CPV* in Eqs. (25) and (26) is expressed in mass units of grams, while the cumulative pore volume $\overline{CPV}$ of mortar and aggregate per unit volume can be determined by

$$\overline{CPV}_{*\_\#} = \rho_* \cdot CPV_{*\_\#} \tag{27}$$

where * represents either m for mortar or g for aggregate; ρ_m denotes the density of mortar, while ρ_g signifies the density of aggregate; # represents either power law distribution or lognormal distribution.

In the atmosphere, concrete's moisture content rapidly increases before gradually leveling off over time (Wang et al., 2017). Free water in concrete has a pore diameter range that both facilitates and hinders penetration. This phenomenon occurs, because free water cannot fill all uniformly sized pore spaces, influenced by the permeation path and pore structure. This investigation found humidity levels around the concrete specimen, reaching 2 to 3 cm above the water level, due to capillary action after immersion and shown in Fig. 14. Wittmann et al. (Wittmann et al., 2012) used neutron radiation to study moisture migration in water-saturated mortar. The research found that free water infiltration from cracks into the mortar skeleton causes varying penetration speeds across different surfaces. Free water ingress into concrete is affected by uneven pore distribution, leading to inconsistent filling.

Fig. 14 Capillary infiltration phenomenon during the saturation process of concrete

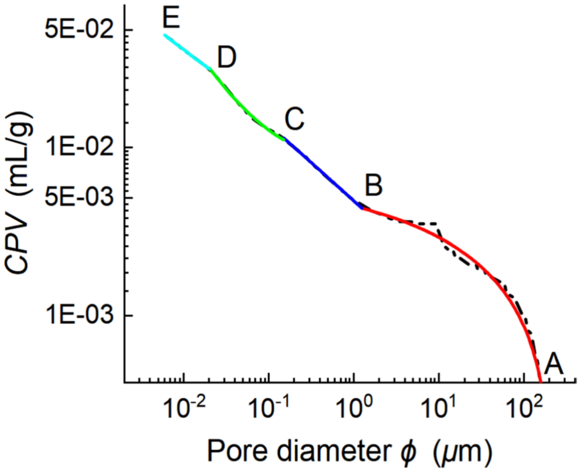

Fig. 15 Division of mortar pores

The cumulative pore curve in Fig. 15 shows that segment AB has an arc-shaped pattern, with pore diameters over 1.25 μm. Most pores exceed 5 μm in diameter and are easily filled with unbound water. This explains water saturation in concrete. The main factor in the rapid increase of water absorption capacity in the initial phase. The BE section shows a linear trend and consists of three stages. The BC section refers to pores with diameters of 0.15 μm to 1.25 μm, mainly the spaces not filled by solid products of hydrated cement paste. The pore walls are irregular and classified as capillary pores. They primarily cause the slow increase in concrete's water absorption during later saturated stages. The DE segment has pore diameters under 0.02 μm and a gelling pore structure. The CD section features pore diameters of 0.02 μm to 0.15 μm. The pore diameter range marks the transition from capillary to gelled pores. Unbound water infiltrates the pores and capillaries, mainly within the AD segment's pore diameter range, as shown in Fig. 15.

Once free water occupies a pore, it can completely fill it. The effective pore water filling ratio is the ratio of the volume of free water in a pore to the total pore volume for a given diameter. This study assumes the effective filling rate of pore space in the lognormal distribution segment filled with free water is 1.0, while in the power law distribution segment, it is less than 1.0. Mortar exhibits three sections of power law distribution, each with varying effective pore water filling rates. Smaller pore sizes result in lower effective filling rates.

4.4 Water Content Model Considering the Characteristics of Concrete Pore Structure

4.4.1 Water Content Model of Wet Concrete

Variations in the pore structures of mortar and aggregate result in disparate moisture levels between the two components in wet concrete. Assuming the volumetric moisture content of the aggregate is denoted as VWC_g and the volumetric moisture content of the mortar as VWC_m, with the volume of aggregate in concrete represented by V_g and the volume of mortar by V_m, the total volume of concrete can be denoted as $V_c = V_g + V_m$, and the total volume of water content in concrete as $V_w = V_g \cdot VWC_g + V_m \cdot VWC_m$.

Assuming that the cumulative pore volume proportion functions of aggregate and mortar from large to small are denoted as $F_g(\phi, \phi_{\max})$ and $F_m(\phi, \phi_{\max})$, respectively, and the total pore volumes of unit volume of aggregate and mortar are represented by V_g^{pore} and V_m^{pore}. When concrete is submerged in water, it is postulated that free water has the ability to entirely occupy the voids with a pore diameter greater than ϕ_w. Consequently, this leads to the situation were

$$VWC_g = V_g^{pore} \cdot F_g(\phi_w, \phi_{\max}) \tag{28a}$$

$$VWC_m = V_m^{pore} \cdot F_m(\phi_w, \phi_{\max}) \tag{28b}$$

Subsequently, the total water content volume in concrete is determined:

$$V_w = V_g \cdot V_g^{pore} \cdot F_g(\phi_w, \phi_{\max}) + V_m \cdot V_m^{pore} \cdot F_m(\phi_w, \phi_{\max}) \tag{29}$$

Dividing both sides of Eq. (29) by V_{con} yields:

$$VWC = p_g \cdot V_g^{pore} \cdot F_g(\phi_w, \phi_{\max}) + p_m \cdot V_m^{pore} \cdot F_m(\phi_w, \phi_{\max}) \tag{30}$$

where p_m and p_g represent the volume proportions of mortar and aggregate in concrete.

The analysis indicates that free water mainly occupies larger pore spaces, leaving smaller ones partially filled. Pore space saturation by unbound water is divided into three categories. The initial segment refers to pore space with diameters over 226 μm, exceeding mercury porosimetry's measurement capability. The total pore volume per unit volume of aggregate is ΔVWC_g, and for mortar, it is ΔVWC_m. This porosity mainly exists in mortar due to incomplete air expulsion during concrete vibration. The second section discusses the pore diameter range with a lognormal distribution of cumulative pore volume, while the third section covers the range with a power-law distribution. Under ambient conditions, the first and second sections may be nearly saturated with free water, while the third section may not reach full saturation. Thus, the pore water distribution model can be adjusted as follows:

$$\begin{aligned} VWC = p_g \cdot \left\{ P_g \cdot \left[\chi_g \cdot F_{g\_powelaw}(\phi_1, \phi_{power\_\max}) + F_{g\_lognormal}(\phi_2, \phi_{226}) \right] + \Delta VWC_g \right\} \\ + p_m \cdot \left\{ P_m \cdot \left[\chi_m \cdot F_{m\_powerlaw}(\phi_1, \phi_{power\_\max}) + F_{m\_lognormal}(\phi_2, \phi_{226}) \right] + \Delta VWC_m \right\} \end{aligned} \tag{31}$$

in which functions $P_g = V_g^{pore}$, $P_m = V_m^{pore}$, $F_{g\_powelaw}(\phi_1, \phi_{power\_\max})$ and $F_{g\_lognormal}(\phi_2, \phi_{226})$ represent the power law distribution and lognormal distribution of pores within the aggregate. Functions $F_{m\_powerlaw}(\phi_1, \phi_{power\_\max})$ and $F_{m\_lognormal}(\phi_2, \phi_{226})$ represent the pore power law distribution and lognormal distribution of the mortar, respectively. χ_g and χ_m represent the efficient filling rates of free water in aggregate and mortar, respectively, falling within the power law distribution range of pores.

In a unit volume of porous media material, the cumulative pore volume $\overline{CPV}$ is defined as the total pore volume multiplied by the cumulative pore volume proportion function:

$$\overline{CPV}_{*\_\#}(\cdot,\cdot) = P_* \cdot F_{*\_\#}(\cdot,\cdot) \tag{32a}$$

or

$$\overline{CPV}_{*\_\#}(\cdot,\cdot) = V_*^{pore} \cdot F_{*\_\#}(\cdot,\cdot) \tag{32b}$$

.

where * represents either m for mortar or g for aggregate, and # represents either power law distribution or lognormal distribution. Equation (31) can be transformed into the following equation:

$$\begin{aligned} VWC = p_g \cdot \Big\{ \sum \chi_g \cdot \overline{CPV}_{g\_powelaw}(\phi_1, \phi_{power\_\max}) \\ + \overline{CPV}_{g\_lognormal}(\phi_2, \phi_{226}) + \Delta VWC_g \Big\} \\ + p_m \cdot \Big\{ \sum \chi_m \cdot \overline{CPV}_{m\_powerlaw}(\phi_1, \phi_{power\_\max}) \\ + \overline{CPV}_{m\_lognormal}(\phi_2, \phi_{226}) + \Delta VWC_m \Big\} \end{aligned} \tag{33}$$

Here, $\sum \cdot$ represents the cumulative sum of the free water volume with different effective porosity ranges.

4.4.2 Distributed Principle of Pore Water in Aggregate and Mortar

Analysis of moisture content data for mortar and aggregate shows that under natural atmospheric conditions, free water cannot fully occupy all the pores. Free water fills large-diameter pores, with the aggregate's pore space measuring 137.6 ~ 226 μm. The material occupies part of the pore space in the lognormal distribution but cannot fill the entire space defined by the power law distribution. The mortar's water content is 0.00623 mL/g. Free water can fill pore spaces in both the lognormal and power law distribution diameter ranges.

In a water pressure environment, concrete has a higher moisture content than in a natural atmosphere. This extra water will permeate the pores of the aggregate and mortar in varying amounts. The pores in the aggregate, which have diameters within the lognormal distribution range and are not fully filled, are likely to be selectively occupied by the newly introduced free water. In a water pressure setting, the mass of fresh free water per gram of aggregate, denoted as the additional mass moisture content Δmwc_g^{pres} of the aggregate, is

$$\Delta mwc_g^{pres} = \Delta m_{con}^{pres} / m_{con}^{atmos} \cdot mwc_g^{atmos} \tag{34}$$

in which, mwc_g^{atmos} represents the moisture content per unit mass of the aggregate in the atmospheric environment for a given concrete specimen; m_{con}^{atmos} denotes the mass of free water absorbed by the concrete in the atmospheric environment; and Δm_{con}^{pres} signifies the additional mass of free water in concrete when subjected to a pressurized water environment in comparison with the natural atmospheric conditions.

In a pressurized water environment, the moisture content Δmwc_m^{pres} of the mortar component of the concrete increases due to the added mass. Adhere to the principle of mass conservation and perform calculations based on Eq. (23):

$$p_g \cdot \rho_g \cdot \Delta mwc_g^{pres} + p_m \cdot \rho_m \cdot \Delta mwc_m^{pres} = \Delta m_{con}^{pres} \tag{35}$$

Following the calculations, when exposed to a water pressure of 3 MPa, the mass moisture content of the aggregate and mortar constituents in concrete is 0.00122 mL/g and 0.00779 mL/g, respectively. Under a water pressure below 5 MPa, the mass moisture content of the aggregate and mortar constituents in concrete is 0.00127 mL/g and 0.00810 mL/g, respectively.

4.4.3 Distributed Parameter of Pore Water

When employing Eq. (35) for ascertaining the pore water distribution parameters of mortar and aggregate in concrete, it is essential to ensure that the water content of both the mortar and aggregate does not exceed the independently measured water content.

The mortar's volume moisture content is 1.397%, and the aggregate's is 0.269%. The theoretical volume moisture content of concrete is determined by the volume proportions of mortar and aggregate. The calculated moisture content was 0.937%, lower than the measured 1.032%. This phenomenon arises from individual mortar specimen pouring, which facilitates the easy escape of air bubbles during vibration. During concrete pouring, aggregate hinders the escape of air bubbles in the mortar. This situation increases porosity. The high porosity of the interface layer between aggregate and mortar leads to a measured moisture content in concrete that is higher than the theoretical value. Enlarged pores in the mortar component exceed 226 μm in diameter. The conserved water content in the mortar is 0.161%. The aggregate is made of granite, known for its high density. $\Delta VWC_g = 0.0\%$ indicates no pore space with a diameter greater than 226 μm.

The pore water distribution parameters for aggregate and mortar in concrete under atmospheric conditions and water pressures of 3 MPa and 5 MPa are shown in Table 2. Pore water volume in aggregates is usually low. During aggregate saturation, air expulsion from pores is hindered, and free water distribution is confined to a logarithmic normal distribution instead of a power law distribution. As water pressure rises, the pore diameter for free water infiltration in the aggregate decreases. Increased water pressure results in greater pore water volume. In mortar, a pore diameter within the lognormal distribution range allows for complete filling of pore spaces by free water, denoted as $\chi_* = 1.0$. If the pore diameter is within the power law distribution range, free water cannot fully occupy the pore space, leading to $\chi_* < 1.0$. As water pressure rises, pore diameter adheres to a power law distribution. Consequently, the effective filling rate of free water in the pores increases, reducing the diameter for pore water permeation. The effective filling rate of free water is higher in pores measuring 0.15 μm to 1.25 μm than in those smaller than 0.15 μm, due to the difficulty of penetration in smaller pores. Free water distribution in pores typically follows fundamental principles and laws. Table 2 indicates that at water pressures of 3 MPa and 5 MPa, free water can infiltrate mortar pores with diameters of about 0.034 μm, consistent with the findings in Zhao et al. (2023).

Table 2 Parameters of free water distribution in pores

Water saturated environment	**Component**	**Power law distribution**			**Lognormal distribution**
		ϕ_1 (μm)	**$\phi_{\text{power max}}$ (μm)**	**χ_***	**ϕ_2 (μm)**
Atmospheric natural environment	Aggregate	–			**137.60**
	Mortar	0.15	1.25	0.20	1.25
		0.0411	0.15	0.045	
3 MPa water pressure	Aggregate	–			**122.70**
	Mortar	0.15	1.25	0.37	1.25
		0.0343	0.15	0.075	
5 MPa water pressure	Aggregate	–			**115.70**
	Mortar	0.15	1.25	0.41	1.25
		0.0338	0.15	0.078	

The bold values are the minimum pore diameters of free water can filled

4.5 Evaluate the Viscous Stress in Concrete

When the pores are entirely filled with free water of uniform diameter, the viscous stress coefficient can be determined using Eq. (12). Subsequently, the viscous stress induced by pore water under varying strain rates can be computed based on Eq. (13). Unbound water is incapable of entirely occupying pores of identical diameters, resulting in an effective filling rate of $\chi_* < 1.0$. Equation (12) can be transformed into Eq. (36) to compute the viscous stress induced by pore water:

$$\tilde{\sigma}_v = \chi_* \cdot VSC \cdot \eta\dot{\varepsilon} \tag{36}$$

4.5.1 Pore Water Viscous Stress in Mortar

The pore diameter in the mortar conforms to the lognormal distribution range, with an effective filling rate of pore water denoted as $\chi_* = 1.0$. The calculation begins with determining the VSC as 2.358×10^7. Subsequently, the viscous stress induced by pore water within a unit volume of mortar under a strain rate of 10^{-2}/s is computed to be 5.551×10^{-4} MPa. This finding is relevant to fully saturated concrete exposed to atmospheric conditions as well as water pressure environments at 3 MPa and 5 MPa.

The pore diameter in the mortar falls within the range of the power law distribution, and the effective filling rate of pore water is $\chi_* < 1.0$. First, based on the pore water distribution parameters outlined in Table 2, it can be observed that under natural atmospheric conditions and water pressure environments of 3 MPa and 5 MPa, free water adheres to distinct pore diameter ranges. Initially, the viscous stress coefficients need to be computed across various pore diameter ranges, along with the viscous stress induced by pore water per unit volume of mortar at a strain rate of 10^{-2}/s. Subsequently, the viscous stress coefficients should be determined for two distinct pore diameter ranges. The cumulative viscous stresses resulting from pore water within the power law distribution range of the mortar under atmospheric natural conditions, as well as under water pressures of 3 MPa and 5 MPa, are calculated to be 6.95 MPa, 23.58 MPa, and 25.98 MPa, respectively.

4.5.2 Pore Water Viscous Stress in Aggregate

The pore diameter within the aggregate conforms to the lognormal distribution range, and the effective filling rate χ_* of pore water is equal to 1.0. The free water adhesion pore diameter ranges vary between the atmospheric environments with water pressure levels of 3 MPa and 5 MPa. The viscous stress coefficients were initially determined as VSC = 25.50, 37.24, and 44.67, and subsequently, the viscous stresses induced by pore water within the unit volume of aggregate at a strain rate of 10^{-2}/s were computed as 0.720×10^{-9} MPa, 1.052×10^{-9} MPa, and 1.262×10^{-9} MPa, respectively.

In the context of aggregates, when subjected to natural atmospheric conditions and water pressures of 3 MPa and 5 MPa, free water is unable to infiltrate the pore diameters falling within the range of power law distribution. Consequently, the VSC is equal to 0, leading to zero viscous stress induced by pore water, which also amounts to 0 MPa.

The mortar's pore diameter is within the lognormal distribution range. Viscous stress from pore water is much lower than that within the pore range governed by a power law distribution. The low moisture content of the aggregate prevents free water from infiltrating the pore diameter range needed to calculate viscous stress. In the lognormal distribution, viscous stress from pore water in aggregates is lower than in mortar. The viscous stress from unbound water in wider pore diameters is minimal, rendering its effect on concrete strength negligible.

The viscous stress from pore water in different mortar diameter ranges was calculated and is presented in Table 3. Analysis shows that as water pressure increases, the pore diameter follows a power law distribution. Furthermore, the effective filling rate of free water in mortar pores and pore water volume increase. In addition, the diameter for pore water penetration decreases. Under equivalent water pressure saturation, reducing the pore diameter range, where free water adheres significantly increase viscous stress, despite lower pore water volume and effective filling rate per unit mass of mortar. Conversely, as pore diameter increases, the volume of pore water also rises. At a filling rate of 1.0, viscous stress is significantly lower.

The analysis indicates that viscous stress from unbound water in larger pores can be ignored. The viscous stress from unbound water in pores larger than 226 μm is negligible. Viscous stress from pore water in the power-law diameter distribution under dynamic loading significantly impacts the mechanical properties of concrete.

4.5.3 Pore Water Viscous Stress in Concrete

Viscous stress from pore water in aggregates and mortar can be calculated by combining the stress from free water with pore diameters in the power law and lognormal distribution ranges. Analyzing the volume proportions of aggregate and mortar in concrete enables the calculation of total viscous stress from pore water in a unit volume, as indicated in Table 4.

Table 5 presents the concrete strength outcomes for loading rate displacements of 10^{-5}/s, 10^{-4}/s, 10^{-3}/s, and 10^{-2}/s in the axial orientation, under dry conditions and water pressures of 3 MPa and 5 MPa. Table 5 demonstrates that higher water pressure correlates with

Table 3 Viscous stress caused by pore water in different diameter ranges in mortar

Water saturated environment	Free water attached pore diameter range (μm)	Effective fill rate χ_*	Pore water volume per unit mass of mortar (mL/g)	Viscous stress (MPa)
Atmospheric natural environment	0.0411 ~ 0.15	0.045	0.000356	6.493
	0.15 ~ 1.25	0.20	0.001354	0.455
	1.25 ~ 226	1.0	0.00452	5.551×10^{-4}
3 MPa water pressure	0.0343 ~ 0.15	0.075	0.0007659	22.769
	0.15 ~ 1.25	0.37	0.002504	0.813
	1.25 ~ 226	1.0	0.00452	5.551×10^{-4}
5 MPa water pressure	0.0338 ~ 0.15	0.078	0.0008012	25.094
	0.15 ~ 1.25	0.41	0.002775	0.883
	1.25 ~ 226	1.0	0.00452	5.551×10^{-4}

Table 4 Pore water viscous stress of concrete

Water saturated environment	Component	Viscous stress (MPa)
Atmospheric natural environment	Aggregate	0.720×10^{-9}
	Mortar	6.95
	Concrete	4.11
3 MPa water pressure	Aggregate	1.052×10^{-9}
	Mortar	23.58
	Concrete	13.96
5 MPa water pressure	Aggregate	1.262×10^{-9}
	Mortar	25.98
	Concrete	15.38

Note: The calculation of viscous stress is at the strain rate $\dot{\varepsilon}$ of 10^{-2}/s

Table 5 Concrete strength (MPa)

Experiment environment	Strain rate			
	10^{-5}/s	10^{-4}/s	10^{-3}/s	10^{-2}/s
Dry	48.3	60.2	64.8	68.2
3 MPa	51.6	66.8	73.6	84.7
5 MPa	54.2	69.0	80.7	87.6

increased concrete strength. The concrete specimen experiences triaxial compression from lateral pressure, enhancing its strength. At a strain rate of 10^{-5}/s, concrete shows strength increases of 3.3 MPa and 5.9 MPa under water pressures of 3 MPa and 5 MPa, respectively, compared to dry conditions. This outcome results from confining pressure, supported by many experiments (Zeng et. al 2013).

Compressive strength of concrete rises with strain rate. Wet concrete shows higher rate sensitivity in strength than dry concrete. Table 5 shows that increasing the strain rate from 10^{-5}/s to 10^{-2}/s results in a 19.9 MPa increase in dry concrete strength. At water pressures of 3 MPa and 5 MPa, concrete strength increases by 33.1 MPa and 33.4 MPa, respectively. Underwater pressure environments greatly enhance concrete strength compared to dry concrete. Wet concrete strength increases primarily from the enhanced skeletal matrix strength and dynamic viscous stress from pore water. The analysis reveals that at water pressures of 3 MPa and 5 MPa, the viscous stress from pore water in concrete under dynamic loading is 13.2 MPa and 13.5 MPa, respectively. This stress level is approximately 27.7% of dry concrete's strength.

In atmospheric conditions, the pore water viscous stress estimated by the refined model is 4.11 MPa, about 8.5% of dry concrete's tensile strength. At water pressures below 3 MPa, the refined model's predicted viscous stress is 5.7% higher than the experimental test results. At water pressures below 5 MPa, the refined model's predicted viscous stress is 13.9% higher than the experimental results in Wang et al., (2016b). The viscous stress calculated with the refined model shows a slight discrepancy from the experimental results but remains closely aligned. This suggests that the model demonstrates strong adaptability.

The viscous stress in the fine model exhibits slight deviation. This phenomenon may be due to the pore structure's "ink bottle " effect. Mercury infiltrates from larger to smaller pores as pressure rises. The "ink-bottle" effect describes how mercury moves from smaller to larger pores. In standard MIP testing, pressurization enables mercury to infiltrate the pore network through throat pores, accessing the internal pores of the sample container (Giesche, 2006; Zeng et al., 2020; Zhou et al., 2010). During decompression, mercury in the throat pores can be expelled, but mercury in the internal pores of the ink bottle becomes irreversibly confined (Diamond 2001; Zhang et al. 2002). Large ink-bottle pores are classified as small pores. Under high-water pressure, concrete's water content is higher than that of concrete saturated in the atmosphere. The volume of unbound water in the ink bottle's pores is expected to increase. Unbound water may have restricted movement, preventing the generation of viscous stress. This study assumes that all free water can generate viscous stress through flow. The viscous stress calculated with the fine model may be overestimated. The refined model in this study is based on the premise of gradually decreasing pore diameters for free water permeation. Free water in the viscous stress from pore water on smaller diameters can overestimate calculated results. Moreover, the shrinkage of concrete increases with age, leading to an increase/rise in pore volume (Tran et al., 2021). When the MIP test is earlier than the water content test and the mechanical test of concrete under water pressure, it will lead to the situation, where the free water permeability pore size estimated by the model in this paper is smaller than the actual permeability of pore water, resulting in an overestimated pore water viscosity stress.

The proposed model is related to pore structure characteristics and distribution characteristics of viscous fluid (e.g., free water) in pore spaces, including effective filling rate and distribution diameter range of free water. However, the characteristics of pore structure are very complex, and there are many measurement methods (Wang et al., 2022), such as X-ray CT, NMR, MIP, gas absorption method, etc. The results of different detection methods also are not completely consistent. The DPVPD expression obtained by which detection method is better to predict the pore water viscous stress needs more extensive research.

In addition, additives such as water reducers and organic polymer modifiers, along with mineral admixtures, such as fly ash and silica fume, alter the pore structure of concrete materials (Tran et al., 2022). These changes also modify the interfacial interactions between pore water and solid pore surfaces, thereby influencing the effective filling rate of free water and the pore diameter distribution range. The proposed model's universal applicability across various types of concrete requires further experimental validation.

5 Summary and Conclusions

A new model is introduced to refine viscous stress by considering pore structure characteristics to estimate stress from viscous liquids like free water. The VSC is quantified by examining the pore structure of the mortar and aggregate. This coefficient is essential for calculating the viscous stress from pore water. A water content model is created to determine the distribution of free water in the pore space, based on the cumulative pore volume curve and water content test results. An analysis of this model yields the following conclusions:

(1) A refined theoretical method is developed from the Stefan effect by including the viscous stress of pore water at different pore diameters. This model clarifies the link between mesoscopic pore structure and the mechanical effects of macroscopic viscous flow. In a singular porous medium, viscous stress from a fluid is the product of the viscous stress coefficient, fluid viscosity, and strain rate.

(2) The viscous stress coefficient relates to pore structure characteristics and the diameter range of pores with attached viscous fluid. It is an integral of the DPVPD. Utilize the data extracted from the mercury porosimeter software to perform direct calculations, and subsequently scale the outcome by a factor of 10^{12} to eliminate the influence of non-uniform length dimensions.

(3) In the logarithmic coordinate system, the CPV curves of mortar and aggregate show similar characteristics. Pore diameters display an arc shape that aligns with a lognormal distribution. Conversely, in a narrower range of pore diameters, it shows a linear pattern and follows a power law distribution. This study effectively characterizes the CPV of mortar and aggregate and indicates that free water can fully occupy pore space when the pore diameter is within the lognormal distribution range, based on the integration of the water content test, CPV, and pore characteristics. Conversely, when the pore diameter is within the power law distribution range, free water cannot fully occupy all pore spaces. A concrete moisture content was developed by examining the pore structure of mortar and aggregate and the distribution of free water in the pores.

(4) The viscous stress of pore water is mainly influenced by free water in smaller pores. Free water adhering to pores within the power law range generates significant viscous stress. Viscous stress from free water on larger pores is negligible relative to the concrete matrix's strength.

(5) This study presents a method to calculate pore water viscous stress in concrete made of mortar and aggregate. It explores the effect of varying effective filling rates on pore water viscous stress. The refined viscous stress model's predictions of concrete behavior closely match experimental results. The calculated viscous stress is slightly higher due to the neglect of the "ink bottle" effect in pore structure analysis.

The refined viscous stress model, derived from Stefan's formulation and assuming pores as circular discs separated by a viscous film, encounters limitations due to the intricate nature of concrete's pore structure. Additives and mineral admixtures can significantly influence pore structure parameters, and despite the model showing strong adaptability, its universal applicability across different concrete types demands more experimental validation. Closely associated with pore structure and free-water distribution, the model is impacted by the addition of various substances that alter pore structure, interfacial interactions, and free-water dynamics. Moreover, factors like drying shrinkage over time and test-method variations affect pore-structure characteristics. To enhance the model, diverse detection methods should be employed to obtain DPVPD and calculate VSC for different concrete types and ages, integrating more pore-structure parameters, and further research should focus on better incorporating material pore-structure features to improve the model's overall applicability.

Acknowledgements
The research reported in this paper was supported by the National Natural Science Foundation of China (Grant Number 51709155, 52079072) and the 111 Project of Hubei Province (Grant Number 2021EJD026).

Author contributions
Qianfeng Wang: conceptualization, supervision, and writing—original draft preparation. Xiaofen Wang: visualization, formal analysis, and investigation. Xinghua Chen: validation, resources, and writing—review and editing. Jie Li: data curation, investigation, and writing—original draft preparation. Jinsheng Lei: methodology and supervision.

Funding
National Natural Science Foundation of China (Grant Number 51709155, 52079072) and the 111 Project of Hubei Province (Grant Number 2021EJD026).

Availability of Data and Materials
All data is provided in full in the results of this paper.

Declarations

Ethics Approval and Consent to Participate
Not applicable.

Consent for Publication
Not applicable.

Competing Interests
The authors declare that they have no known competing financial interests or personal relationships that could have appeared to influence the work reported in this paper.

Received: 18 February 2025 Accepted: 1 June 2025

References

Cadoni, E. (2005). Strain-rate effect on the tensile behaviour of concrete at different relative humidity levels. *Materials and Structures, 34*(1), 21–26. https://doi.org/10.1007/BF02482196

Diamond, S. (2000). Reply to the discussion by S. Chatterji of the paper "Mercury porosimetry—an inappropriate method for the measurement of pore size distributions in cement—based materials." *Cement and Concrete Research, 31*(11), 1659. https://doi.org/10.1016/s0008-8846(01)00619-6

Frías, M., & de Rojas, M. I. S. (1997). Microstructural alterations in fly ash mortars: Study on phenomena affecting particle and pore size. *Cement and Concrete Research, 27*(5), 619–628. https://doi.org/10.1016/s0008-8846(97)00026-4

Gangopadhyay, K., & Basu, B. (2009). City size distributions for India and China. *Physica a: Statistical Mechanics and Its Applications, 388*(13), 2682–2688. https://doi.org/10.1016/j.physa.2009.03.019

Giesche, H. (2006). Mercury porosimetry: A general (practical) overview. *Particle & Particle Systems Characterization, 23*(1), 9–19. https://doi.org/10.1002/ppsc.200601009

Kagan, Y. Y. (2010). Earthquake size distribution: Power-law with exponent $\beta \equiv 1/2$? *Tectonophysics, 490*(1–4), 103–114. https://doi.org/10.1016/j.tecto.2010.04.034

Kaji, T., & Fujiyama, C. (2014). Mechanical properties of saturated concrete depending on the strain rate. *Procedia Engineering, 95*, 442–453. https://doi.org/10.1016/j.proeng.2014.12.204

Kaplan, S. A. (1980). Factors affecting the relationship between rate of loading and measured compressive strength of concrete. *Magazine of Concrete Research, 32*(111), 79–88. https://doi.org/10.1680/macr.1980.32.111.79

Kayyali, O. A. (1985). Mercury intrusion porosimetry of concrete aggregates. *Materials and Structures, 18*(3), 259–262. https://doi.org/10.1007/bf02472913

Kumar, R., & Bhattacharjee, B. (2003). Porosity, pore size distribution and in situ strength of concrete. *Cement and Concrete Research, 33*(2), 155–164. https://doi.org/10.1016/s0008-8846(02)00942-0

Li, L., Zhang, H., Guo, X., Zhou, X., Lu, L., Chen, M., et al. (2019). Pore structure evolution and strength development of hardened cement paste with super low water-to-cement ratios. *Construction and Building Materials, 227*, Article 117108. https://doi.org/10.1016/j.conbuildmat.2019.117108

Liang, J., Wang, Q., Zhang, X., & Xiao, Y. (2020). Study on water content and dynamic mechanical properties of fly ash concrete under water confining pressure. *Hydro Science and Engineering, 6*(2), 115–120. https://doi.org/10.12170/20191010002

Malamud, B. D., & Turcotte, D. L. (2006). The applicability of power-law frequency statistics to floods. *Journal of Hydrology, 322*(1–4), 168–180. https://doi.org/10.1016/j.jhydrol.2005.02.032

Mehta, P. K., & Monteriro, P. J. M. (2006). *Concrete: Microstructure, properties, and materials*. McGraw-Hill.

Newman, M. (2005). Power laws, pareto distributions and Zipf's law. *Contemporary Physics, 46*(5), 323–351. https://doi.org/10.1080/00107510500052444

Pedersen, R. R., Simone, A., & Sluys, L. J. (2008). An analysis of dynamic fracture in concrete with a continuum visco-elastic visco-plastic damage model. *Engineering Fracture Mechanics, 75*(12), 3782–3805. https://doi.org/10.1016/j.engfracmech.2008.02.004

Pedersen, R. R., Simone, A., & Sluys, L. J. (2013). Mesoscopic modeling and simulation of the dynamic tensile behavior of concrete. *Cement and Concrete Research, 50*, 74–87. https://doi.org/10.1016/j.cemconres.2013.03.021

Reinhardt, H. W., Rossi, P., & van Mier, J. G. (1990). Joint investigation of concrete at high rates of loading. *Materials and Structures, 23*(3), 213–216. https://doi.org/10.1007/bf02473020

Rossi, P. (1991a). Influence of cracking in the presence of free water on the mechanical behaviour of concrete. *Magazine of Concrete Research, 43*(154), 53–57. https://doi.org/10.1680/macr.1991.43.154.53

Rossi, P. (1991b). A physical phenomenon which can explain the mechanical behaviour of concrete under high strain rates. *Materials and Structures, 24*(5), 422–424. https://doi.org/10.1007/bf02472015

Rossi, P., & Toutlemonde, F. (1996). Effect of loading rate on the tensile behaviour of concrete: Description of the physical mechanisms. *Materials and Structures, 29*(2), 116–118. https://doi.org/10.1007/bf02486201

Ross, C. A., Jerome, D. M., Tedesco, J. W., & Hughes, M. L. (1996). Moisture and strain rate effects on concrete strength. *ACI Materials Journal, 93*(3), 293–300. https://doi.org/10.14359/9814

Stephen, A. T., & Toubia, O. (2009). Explaining the power-law degree distribution in a Social Commerce Network. *Social Networks, 31*(3), 262–270. https://doi.org/10.1016/j.socnet.2009.07.002

Sun, X., Wang, H., Cheng, X., & Sheng, Y. (2020). Effect of pore liquid viscosity on the dynamic compressive properties of concrete. *Construction and Building Materials, 231*, Article 117143. https://doi.org/10.1016/j.conbuildmat.2019.117143

Tran, N. P., Gunasekara, C., Law, D. W., et al. (2021). A critical review on drying shrinkage mitigation strategies in cement-based materials. *Journal of Building Engineering, 38*, Article 102210. https://doi.org/10.1016/j.jobe.2021.102210

Tran, N. P., Nguyen, T. N., & Ngo, T. D. (2022). The role of organic polymer modifiers in cementitious systems towards durable and resilient infrastructures: A systematic review. *Construction and Building Materials, 360*, Article 129562. https://doi.org/10.1016/j.conbuildmat.2022.129562

Wang, H., Jin, W., & Li, Q. (2009). Saturation effect on dynamic tensile and compressive strength of concrete. *Advances in Structural Engineering, 12*(2), 279–286. https://doi.org/10.1260/136943309788251713

Wang, H., & Li, Q. (2007a). Experiments of the compressive properties of dry and saturated concrete under different loading rates. *Journal of Hydroelectric Engineering, 26*(1), 84–89. https://doi.org/10.1007/s10870-007-9222-9

Wang, H., & Li, Q. (2007b). Experiments on saturated concrete under different splitting tensile rate and mechanism on strength change. *Engineering Mechanics, 24*(1), 105–109. https://doi.org/10.1142/S1016237207000148

Wang, H., Wang, L., Song, Y., & Wang, J. (2016a). Influence of free water on dynamic behavior of dam concrete under biaxial compression. *Construction and Building Materials, 112*, 222–231. https://doi.org/10.1016/j.conbuildmat.2016.02.090

Wang, Q., Liu, Y., & Peng, G. (2016b). Effect of water pressure on mechanical behavior of concrete under dynamic compression state. *Construction and Building Materials, 125*, 501–509. https://doi.org/10.1016/j.conbuildmat.2016.08.058

Wang, Q., Liu, Y., & Peng, G. (2017). Water content in concrete under water pressure environment and the effect on its mechanical properties. *Journal of Hydraulic Engineering, 48*(2), 193–202. https://doi.org/10.13243/j.cnki.slxb.20160539

Wang, J., Dong, S., Zhou, C., et al. (2021). Investigating pore structure of nano-engineered concrete with low-field nuclear magnetic resonance. *Journal of Materials Science, 56*, 243–259. https://doi.org/10.1007/s10853-020-05268-0

Wang, J., Dong, S., Dai Pang, S., et al. (2022). Pore structure characteristics of concrete composites with surface-modified carbon nanotubes. *Cement and Concrete Composites, 128*, Article 104453. https://doi.org/10.1016/j.cemconcomp.2022.104453

Wang, J., Wang, X., Ding, S., et al. (2023). Micro-nano scale pore structure and fractal dimension of ultra-high performance cementitious composites modified with nanofillers. *Cement and Concrete Composites, 141*, Article 105129. https://doi.org/10.1016/j.cemconcomp.2023.105129

Wittmann, F. H., Roelfstra, P. E., Mihashi, H., Huang, Y. Y., Zhang, X. H., & Nomura, N. (1987). Influence of age of loading, water-cement ratio and rate of loading on fracture energy of concrete. *Materials and Structures, 20*(2), 103–110. https://doi.org/10.1007/bf02472745

Wittmann, F. H., Zhang, P., & Zhao, T., et al. (2012). Relation between mass flow in cement-based composite materials and durability investigated by neutron imaging. In Alexander (Ed.), *Concrete Repair Rehabilitation and Retrofitting III* (pp. 476–481). London: Taylor & Francis Group.

Wu, S., Chen, X., & Zhou, J. (2012). Influence of strain rate and water content on mechanical behavior of Dam concrete. *Construction and Building Materials, 36*, 448–457. https://doi.org/10.1016/j.conbuildmat.2012.06.046

Yan, D., & Lin, G. (2008). Influence of initial static stress on the dynamic properties of concrete. *Cement and Concrete Composites, 30*(4), 327–333. https://doi.org/10.1016/j.cemconcomp.2007.11.004

Zeng, Q., Chen, S., Yang, P., Peng, Y., Wang, J., Zhou, C., et al. (2020). Reassessment of mercury intrusion porosimetry for characterizing the pore structure of cement-based porous materials by monitoring the Mercury entrapments with X-ray computed tomography. *Cement and Concrete Composites, 113*, Article 103726. https://doi.org/10.1016/j.cemconcomp.2020.103726

Zeng, Q., Li, K., Fen-Chong, T., & Dangla, P. (2012). Analysis of pore structure, contact angle and pore entrapment of blended cement pastes from Mercury porosimetry data. *Cement and Concrete Composites, 34*(9), 1053–1060. https://doi.org/10.1016/j.cemconcomp.2012.06.005

Zeng, S., Ren, X., & Li, J. (2013). Triaxial behavior of concrete subjected to dynamic compression. *Journal of Structural Engineering, 139*(10), 1582–1592. https://doi.org/10.1061/(ASCE)ST.1943-541X.0000686

Zhang, Y., Hu, D., Li, Y., Yao, H., & Li, X. (2015). Dynamic mechanical properties of dry and saturated concretes and their mechanism. *Explosion and Shock Waves, 35*(6), 864–870. https://doi.org/10.11883/1001-1455(2015)06-0864-07

Zhang, Y., Wu, K., Yang, Z., & Ye, G. (2022). A reappraisal of the ink-bottle effect and pore structure of cementitious materials using intrusion-extrusion cyclic mercury porosimetry. *Cement and Concrete Research, 161*, Article 106942. https://doi.org/10.1016/j.cemconres.2022.106942

Zhao, X., Tian, Y., Zhou, J., & Chai, Z. (2023). Experimental investigation on the effect of high-pressure water on tensile strength and microstructure of cementitious materials. *Construction and Building Materials, 364*, Article 129932. https://doi.org/10.1016/j.conbuildmat.2022.129932

Zheng, D. (2004). An explanation for rate effect of concrete strength based on fracture toughness including free water viscosity. *Engineering Fracture Mechanics, 71*(16), 2319–2327. https://doi.org/10.1016/j.engfracmech.2004.01.012

Zheng, D., Liang, Y., & Li, X. (2021). Influence mechanism of pore liquid viscosity on concrete strength under dynamic loading. *Journal of Hydroelectric Engineering, 40*(6), 152–159. https://doi.org/10.11660/slfdxb.20210614

Zhou, J., Ye, G., & van Breugel, K. (2010). Characterization of pore structure in cement—based materials using pressurization—depressurization cycling mercury intrusion porosimetry (PDC-MIP). *Cement and Concrete Research, 40*(8), 1120–1128. https://doi.org/10.1016/j.cemconres.2010.02.011

Zhou, Z., Cai, X., Zhao, Y., Chen, L., Xiong, C., & Li, X. (2016). Strength characteristics of dry and saturated rock at different strain rates. *Transactions of Nonferrous Metals Society of China, 26*(7), 1919–1925. https://doi.org/10.1016/s1003-6326(16)64314-5

Publisher's Note

Qianfeng Wang Associate professor, PhD, Hubei Key Laboratory of Disaster Prevention and Mitigation and College of Civil Engineering & Architecture, China Three Gorges University, Yichang, 443002, China.

Xiaofen Wang Graduate student, College of Civil Engineering & Architecture, China Three Gorges University, Yichang, 443002, China.

Xinghua Chen Lecturer, PhD, Hubei Key Laboratory of Disaster Prevention and Mitigation and College of Civil Engineering & Architecture, China Three Gorges University, Yichang, 443002, China.

Jie Li Graduate student, College of Civil Engineering & Architecture, China Three Gorges University, Yichang, 443002, China.

Jinsheng Lei Professor, PhD, Hubei Key Laboratory of Disaster Prevention and Mitigation and College of Civil Engineering & Architecture, China Three Gorges University, Yichang, 443002, China.